



HAL
open science

1-Hexene Ozonolysis across Atmospheric and Combustion Temperatures via Synchrotron-Based Photoelectron Spectroscopy and Chemical Ionization Mass Spectrometry

Caroline Smith Lewin, Avinash Kumar, Olivier Herbinet, Philippe Arnoux, Rabbia Asgher, Shawon Barua, Frédérique Battin-Leclerc, Sana Farhoudian, Gustavo Garcia, Luc-Sy Tran, et al.

► **To cite this version:**

Caroline Smith Lewin, Avinash Kumar, Olivier Herbinet, Philippe Arnoux, Rabbia Asgher, et al.. 1-Hexene Ozonolysis across Atmospheric and Combustion Temperatures via Synchrotron-Based Photoelectron Spectroscopy and Chemical Ionization Mass Spectrometry. *Journal of Physical Chemistry A*, 2024, 128 (27), pp.5374-5385. 10.1021/acs.jpca.4c02687 . hal-04732661

HAL Id: hal-04732661

<https://hal.science/hal-04732661v1>

Submitted on 11 Oct 2024

HAL is a multi-disciplinary open access archive for the deposit and dissemination of scientific research documents, whether they are published or not. The documents may come from teaching and research institutions in France or abroad, or from public or private research centers.

L'archive ouverte pluridisciplinaire **HAL**, est destinée au dépôt et à la diffusion de documents scientifiques de niveau recherche, publiés ou non, émanant des établissements d'enseignement et de recherche français ou étrangers, des laboratoires publics ou privés.

1 **1-Hexene Ozonolysis Across Atmospheric and Combustion Temperatures via Synchrotron-**
2 **Based Photoelectron Spectroscopy and Chemical Ionization Mass Spectrometry**

3
4 Caroline Smith Lewin^a, Avinash Kumar^d, Olivier Herbinet^a, Philippe Arnoux^a, Rabbia Asgher^d,
5 Shawon Barua^d, Frédérique Battin-Leclerc^a, Sana Farhoudian^d, Gustavo A. Garcia^b, Luc-Sy
6 Tran^c, Guillaume Vanhove^c, Laurent Nahon^b, Matti Rissanen^{d, e}, and Jérémy Bourgalais*^a

7
8 ^aUniversité de Lorraine, CNRS, LRGP, F-54000 Nancy, France

9 ^bSynchrotron SOLEIL, L'Orme des Merisiers, 91192 Gif-sur-Yvette Cedex, France

10 ^cUniversité Lille, CNRS, PC2A, F-59000 Lille, France

11 ^dAerosol Physics Laboratory, Tampere University, FI-33101, Tampere, Finland

12 ^eDepartment of Chemistry, University of Helsinki, FI-00014, Helsinki, Finland

13
14
15
16
17
18
19
20
21
22
23
24
25
26
27
28
29 *Corresponding author: Jérémy Bourgalais

30 e-mail: jeremy.bourgalais@cnrs.fr

31 ORCID: 0000-0003-4710-8943

32 Phone: (33)3-72-74-38-17

33

34

Abstract

35

36

37

38

39

40

41

42

43

44

45

46

47

48

49

50

51

52

53

Keywords

54

55

This study investigates the complex interaction between ozone and the autoxidation of 1-hexene over a wide temperature range (300 – 800 K), overlapping atmospheric and combustion regimes. It is found that atmospheric molecular mechanisms initiate the oxidation of 1-hexene from room temperature up to combustion temperatures, leading to the formation of highly oxygenated organic molecules. As temperature rises, the highly oxygenated organic molecules contribute to radical-branching decomposition pathways inducing a high reactivity in the low temperature combustion region, i.e. from 550 K. Above 650 K, the thermal decomposition of ozone into oxygen atoms becomes the dominant process, and a remarkable enhancement of the conversion is observed due to their diradical nature, counteracting the significant negative temperature coefficient behavior usually observed for 1-hexene. In order to better characterize the formation heavy oxygenated organic molecules at the lowest temperatures, two analytical performant methods have been combined for the first time: synchrotron-based mass-selected photoelectron spectroscopy and orbitrap chemical ionization mass spectrometry. At the lowest studied temperatures (below 400 K), this analytical work has demonstrated the formation of the ketohydroperoxides usually found during the LTC oxidation 1-hexene, as well as of molecules containing up to 9 O-atoms.

Autoxidation, Highly Oxygenated Organic Molecules, Synchrotron Radiation, Photoelectron Spectroscopy, Quantum Chemistry, Chemical Ionization Mass Spectrometry

56 Introduction

57 The intricacies of the combustion of organic compounds at low-temperature, i.e.
58 from 550 K, so called Low-Temperature Combustion (LTC), are fundamental in
59 comprehending environmental dynamics and promoting energy efficiency. A key aspect of
60 this is the autoxidation of fuel components and of volatile organic compounds (VOCs). This
61 process has repercussions on both atmospheric pollution and combustion pathways ¹⁻⁷.
62 Central to VOC oxidation are repeated radical-chain reactions, initiated by the formation of
63 carbon-centered radicals (R) from organic species (RH) ⁸⁻¹⁰.

64 The rate at which VOCs oxidize is notably temperature dependent. Above 500 K, the
65 oxidation accelerates via sequences of intramolecular H-shift/O₂-addition reactions
66 producing, via successive isomerization of peroxy (ROO) radicals into hydroperoxyalkyl
67 (QOOH) radicals, oxygenated intermediates whose exothermic decomposition enriches the
68 radical pool ¹¹. However, for most of the aliphatic hydrocarbons, there is a twist: beyond a
69 certain temperature threshold ~ 650 K, the negative temperature-coefficient (NTC)
70 emerges ¹², causing an unexpected dip in rates of branching reactions responsible for
71 propagation (QOOH oxidation, cyclic ether decomposition) as temperatures soar further
72 ^{13,14}. The implications of this NTC behavior are substantial, shaping both the efficiency and
73 reliability of combustion, and consequently guiding the evolution of energy devices.

74 At ambient temperature, it was historically posited that VOC autoxidation had
75 minimal impact at ambient temperatures, stemming from the belief that peroxy ROO radical
76 reactions were primarily terminated by chain-ending events and that high C-H bond
77 strengths prevent fast ROO H-migrations under standard conditions ¹⁵. A more detailed
78 analysis, however, reveals that the series of ROO \rightarrow QOOH reactions lead to much higher
79 oxygen contents with the formation of highly oxygenated organic molecules (HOMs) usually
80 defined as containing six or more oxygen atoms ¹⁶. This transformation is influenced by
81 temperature and the presence of substituents, such as -OH, C=C, and C=O, in ROO radical
82 structures ^{17,18}. Although there exists other oxidation mechanisms in the troposphere, ozone
83 (O₃) initiated oxidation of VOC via ozonolysis has been shown to have the highest HOM
84 yields ¹⁶.

85 In contrast to its relevance in atmospheric sciences, O₃ has only recently been
86 identified as a species of interest in combustion chemistry ¹⁹. In the case of saturated
87 reactants, O₃ acts as a promoter for oxidation reactions at combustion-relevant

88 temperatures due to the production of O-atoms from O₃-thermal decomposition. O-atoms
89 readily assist in H-abstraction to initiate VOC oxidation at temperatures lower than in LTC
90 chemistry^{20–23}. For fuels presenting a NTC behavior, this can be significantly reduced by the
91 presence of O-atoms, as it has been shown in the case of dimethylether²⁴,
92 methylhexanoate²⁵, and propane²³. In the case of unsaturated reactants, the interest of
93 ozonolysis mechanism for combustion has received much less attention^{26–28}. While in this
94 case the impact of O₃ is not limited to merely hastening reactions as ozonolysis profoundly
95 alters kinetic networks by modifying molecular structures, the influence of O₃ on fuel
96 reactivity has only been investigated for ethylene²⁹ and methylcrotoate³⁰, two fuels which do
97 not present a NTC behavior.

98 The chemistry of autoxidation systems, particularly those initiated by O₃, is highly
99 complex. This complexity arises from the formation of numerous reactive intermediates that
100 can be present in only trace amounts and that result from various radical reaction pathways
101 influenced by temperature. This work presents an investigation over a wide temperature
102 range (300–800 K) of the influence of O₃ addition on the autoxidation chemistry of 1-
103 hexene (C₆H₁₂), a representative aliphatic compound in surrogate gasoline fuels^{31–33},
104 presenting a notable NTC behavior³⁴. The accuracy of chemical kinetic models depends on
105 experimental data used for both identifying and structurally characterizing these species;
106 however, obtaining reliable data is difficult using only a single analytical tool. As this work
107 especially focuses on product identification, an orbitrap mass spectrometer equipped with a
108 multi-scheme chemical ionization inlet (O-MION-CIMS) has been used to detect trace species
109 such as HOMs while a spectrometer using a photoelectron photoionization coincidence
110 scheme coupled to synchrotron radiation (SVUV-PEPICO) has been used to detect lower
111 oxygenated species.

112

113 **Experimental and theoretical methods**

114 This part describes the three experimental setups, a Jet-Stirred Reactor (JSR)³⁵ with
115 analysis using gas chromatographs (GCs), a JSR coupled to mass spectrometry with i²PEPICO
116 spectroscopy, and a Tubular Flow Reactor (TFR) with orbitrap Chemical Ionization Mass
117 Spectrometry (O-CIMS), as well as the related theoretical calculations needed to analyze the
118 obtain data.

119

120
121
122
123
124
125
126
127
128
129
130
131
132
133
134
135
136
137
138
139
140
141
142
143
144
145
146
147
148
149
150

JSR + GCs

This spherical JSR, used by LRGP to study the oxidation of 1-hexene is made from fused silica, has a volume of roughly 81.2 cm³, and is maintained at isothermal and isobaric conditions.³⁵ Gas blends of fuel and O₂ with and without O₃ continuously flows in, with a significant inert gas dilution to counteract the temperature variations from the exothermic oxidation. The reactants are introduced into the JSR using helium as a transport gas, via four central cross-shaped nozzles. These nozzles are designed to enhance turbulence and ensure a homogeneous mixture. There is a preheating section before the reactor's entrance to diminish internal temperature variations. Both the JSR and this preheating section are heated by thermocoax resistances. A K-type thermocouple, located near the center of the JSR in a glass sleeve, monitors the temperature, boasting an accuracy of about 1%. Gases resulting from oxidation in the JSR are conveyed through heated tubes to a pair of GCs for examination. These tubes are made of stainless steel, with an external diameter of 1/8 inch and a length of approximately 5 meters.

At LRGP, the gas leaving the reactor are analyzed thanks to two GCs. The first GC has a carbosphere-packed column and utilizes a thermal conductivity detector (TCD) to measure lightweight and permanent gas species. The second GC comes with a Q-Bond capillary column and a flame ionization detector (FID) which is preceded by a methanizer. This GC specializes in measuring organic compounds. The methanizer contains a hydrogenation Ni bed catalyst. A mix of buffer gas and H₂ (also utilized for the FID) passes through this catalyst, turning species with carbonyl groups into their respective alkanes and converting CO and CO₂ into methane. To identify different species, the GC with the Q-Bond capillary column was paired with a quadrupole mass spectrometer. Ion generation was achieved using electron impact ionization at 70 eV.

Calibrations for FID and TCD were carried out with gaseous standards supplied by Air Liquide for O₂, CH₄, CO, and CO₂. Any other species that the FID detected were calibrated using the effective carbon number (ECN) approach.³⁶ Calibration factors for these species were derived from those of the calibrated ones, factoring in their effective carbon number. The estimated relative uncertainties for species calibrated with gaseous standards stood at

151 $\pm 5\%$. For species calibrated via the ECN approach, the uncertainties were estimated to be
152 around $\pm 10\%$.

153 *JSR + i^2 PEPICO spectroscopy*

154 The same heated JSR was positioned within the SAPHIRS chamber's permanent end-
155 station,³⁷ found at one of the DESIRS VUV beamline's monochromatized branches at the
156 SOLEIL synchrotron.³⁸ There, the JSR's internal gas mixture was extracted through a
157 micrometer-sized hole, facilitating a molecular-beam expansion in the vacuum chamber with
158 a pressure of approximately 10^{-4} mbar. This chamber was linked through two sequential
159 skimmers to the ionization chamber. This process produced a cooled molecular beam where
160 the likelihood of reactive collisions was significantly reduced due to its low number density
161 and dilution with helium. As a result, reactive intermediates were maintained throughout
162 the expansion and made their way to the ionization chamber without any collisions.

163 Within the ionization chamber, the VUV synchrotron light targeted the gas mix,
164 leading to the formation of photoelectrons and photoions. These were detected
165 simultaneously by the double-imaging photoelectron/photoion (i^2 PEPICO) spectrometer
166 known as DELICIOUS III.³⁹ These particles moved in opposite directions, diverging based on
167 their kinetic energies before arriving at the velocity map imaging (VMI) spectrometer,
168 forming circular patterns. The particles' times of arrival were documented. Using the
169 electron's time of arrival as a benchmark, mass spectra were plotted. With the help of the
170 VMI system and photoion-mass selection, a two-dimensional matrix of mass-selected
171 photoelectron spectra (PES) could be created based on photon energy,⁴⁰ using the Abel
172 inversion method. By choosing a specific kinetic energy range (100 meV in this study), the
173 corresponding threshold photoelectron spectra (TPES) could be deduced, specifically within
174 a photon energy span from 9.0 to 10.4 eV, advancing in 10 meV increments with each step
175 taking 60 seconds. The error margins in TPES were calculated using a Poisson distribution of
176 the photoelectron image pixel counts. This was carried through the image's Abel inversion
177 transformation using standard error propagation equations. In TPES, the clarity of the signal
178 can be affected by the occurrence of false coincidences when two or more ionization
179 incidents happen nearly simultaneously. This can obscure the identification of lesser species
180 when the actual coincidence signal aligns with the background's Poisson noise. In scenarios
181 where the signal-to-background ratio is insufficient for an electron kinetic energy analysis,
182 the total ion yield (TIY) for each mass is determined by integrating over all electron energies.

183 TPES provides a glimpse into the isomers' electronic structures. These isomers can be
184 pinpointed by comparing them to the reference spectra of individual entities. If reference
185 spectra are not present in existing studies, the PES of specific entities can be modeled using
186 advanced theoretical computations.

187

188 *TFR + O-CIMS*

189 Gas-phase ozonolysis initiated 1-hexene oxidation was studied in a borosilicate glass
190 flow tube reactor (5 cm o.d. and 100 cm length) coupled with the multi-scheme chemical
191 ionization inlet (MION, Karsa Inc.)^{41,42} and an orbitrap MS (ThermoScientific Exploris 240).
192 The MION inlet was operated with nitrate (NO_3^-) ionization scheme. The 1-hexene (Sigma
193 Aldrich >99% purity) was used from a premixed gas cylinder with a concentration of 100.6
194 ppm diluted in scientific grade N_2 . The O_3 in the experiments was produced by an ozone
195 generator (UVP Ozone Generator, Analytik Jena US), from a 2 SLPM flow of purified air
196 (AADCO 737-15), which was also utilized as the bath gas in the experiments. A total flow rate
197 of around 15 SLPM was applied, with the reaction time controlled by a moveable injector for
198 reagent gas introduction and resulted in 1.5 to 9.2 seconds residence times. All flows were
199 regulated by calibrated mass flow controllers (Alicat Scientific). In a set of experiments D_2O
200 was added to the gas stream to provide further verification on the detected product
201 identities. The $\text{C}_5\text{H}_9\text{O}_7$ radical and its OH loss product $\text{C}_5\text{H}_8\text{O}_6$ both exchanged 2 H to D, and
202 the preceding $\text{C}_5\text{H}_9\text{O}_5$ radical 1 H to D, in accordance with their proposed production
203 pathway (see Figure 3 in the main text). Importantly, the conversion of the reagent ion
204 adduct $\text{HNO}_3 \cdot \text{NO}_3^-$ to $\text{DNO}_3 \cdot \text{NO}_3^-$ was complete, indicating that the H to D exchange of the
205 reaction products also run to competition (i.e., every labile H-atom was quantitatively
206 converted to D-atoms).

207

208 *Theoretical calculations*

209 In this work, we utilized the Merck molecular force field MMFF94 methodology to
210 create initial conformer structures for each isomer considered.⁴³ These were further refined
211 using a superior theoretical approach, namely density functional theory (DFT) with the M06-
212 2X-D3 functional.⁴⁴ This DFT functional was paired with the aug-cc-pVTZ Dunning's
213 correlation consistent basis set,⁴⁵ enhanced with diffuse functions. Additionally, the zero-
214 damped D3 dispersion correction developed by Grimme and colleagues⁴⁶ was integrated

215 into M06-2X. The refined neutral species structures then served as starting points for the
216 ionic forms. We employed two-electron integrals with strict optimization criteria to
217 guarantee the dependability of conformer energies and vibrational frequencies. These were
218 computed within the harmonic approximation at the consistent theoretical level.

219 The refined individual structures underwent conformational averaging through
220 Boltzmann weighting, considering electronic energies and a JSR temperature of 400 K. For
221 this study, it's assumed that all reactants and products stabilize at 400 K. Additionally, the
222 conformer distribution remains constant after expansion via the pinhole. To model
223 transitions between the vibrational stages of the most stable neutral conformers and their
224 ions, we used the time-independent adiabatic Hessian Franck-Condon (TI-AH|FC) model at
225 400 K.⁴⁷ The derived stick spectrum was then combined with a Gaussian profile featuring a
226 200 cm⁻¹ bandwidth, aligning with the experimental resolution. The adiabatic ionization
227 energy (AIE) calculations were conducted at the CBS-QB3 theoretical level, originating from
228 the foundational state of both neutral and ionic forms, and using the refined DFT structures.
229^{48,49} We aligned the 0-0 transition of the computed stick spectra to correspond with the
230 experimental spectra, keeping within the energy calculation's uncertainty.

231 It's crucial to highlight that when examining flexible molecular constructs, such as
232 hydroperoxides, the TPES analysis faces complications. These stem from the existence of
233 vibrational modes with low frequencies. Often, these lead to minimal overlaps between
234 vibrational wave functions, which dilutes the vibrational information. Combined with a
235 diminished signal-to-noise ratio, potential erroneous peaks, and a considerable count of
236 potential isomers, individual assignments become complex. Thus, while simulated spectra
237 are helpful in deducing key elements from experimental spectra, they might not capture all
238 conceivable molecular formations.

239

240 **Experimental Results and Theoretical Analysis**

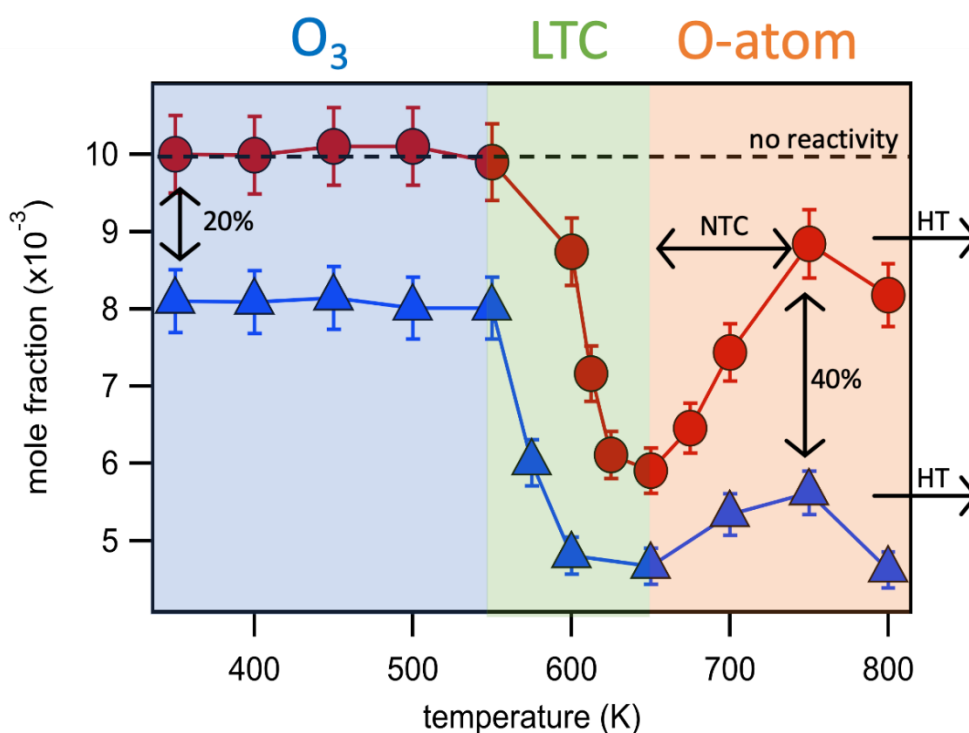
241 This part describes the results obtained for the temperature evolution of 1-hexene
242 mole fraction in JSR and then focuses on the ozonolysis products measured both in TFR and
243 JSR with discussing only a few products measured by GC; the full details of product
244 formation will be given in a future paper.

245

246 *JSR 1-hexene reactivity*

247 This research first examined the reactivity of 1-hexene during its JSR oxidation with
 248 and without O₃ in JSR using GCs. Experiments were conducted over a temperature range of
 249 350-800 K with constant parameters: pressure at 800 torr, equivalence ratio of 0.5, and a
 250 0.01 initial mole fraction of 1-hexene diluted in He. Residence times were 2.0 s (without O₃)
 251 and 2.5 s (with O₃). An O₃ mole fraction of 1,000 ppm was introduced through an O₃
 252 generator using an O₂/He mixture, and its mole fraction quantified by an O₃ analyzer (a
 253 scheme of the experimental setup can be found in Smith Lewin et al. ²⁷). The overall mole
 254 fraction of O₂ is less than 10%.

255 Reactants and products from 350 to 800 K were identified and using two GCs.
 256 1-hexene mole fraction profiles are depicted in Figure 1. The O₃-profile is not shown because
 257 it is almost consumed at 350 K in its reaction with 1-hexene via ozonolysis, despite having a
 258 low rate coefficient ($\sim 10^{-17} \text{ cm}^3 \text{ s}^{-1}$).



259
 260 **Figure 1.** Temperature evolution of the 1-hexene mole fraction as measured by GC during the oxidation
 261 of a reactive gas mixture composed of 1-hexene/O₂/He, with (blue triangles) and without (red dots) O₃ with
 262 figures indicating the conversion yield due to O₃ addition. The blue- and orange-colored areas indicate the
 263 temperature ranges where specific species contribute to the increased conversion of 1-hexene when O₃ is
 264 added. The green area symbolizes the LTC zone.

265

266 Without O₃, the results align with literature regarding the oxidation of 1-hexene³⁴.
267 The beginning of reactivity is observed at 550 K, indicating the transition into the LTC region.
268 At this point, the conversion rate peaks at 40% when the temperature reaches 650 K.
269 Following this, as the system enters the NTC zone, the fuel conversion dropping to as low as
270 10% at 750 K. Subsequently, the reactivity increases significantly upon entering the high-
271 temperature (HT) zone.

272 When O₃ is added, the 1-hexene consumption goes to 20% between 350 and 550 K
273 compared to the case without O₃ where no reactivity is observed before 550 K. This
274 enhancement remains consistent above 550 K. Above 650 K (in the NTC zone), the
275 enhancement increases with temperature, up to 40% at 750 K, making a significant boost in
276 reactivity compared to the non-O₃ case. This enhancement is more marked than for other
277 fuels (dimethylether²⁴, methylhexanoate²⁵, and propane²³), for which such an O₃ effect was
278 reported.

279

280 *1-hexene ozonolysis products in TFR*

281 To understand the 20% reactivity enhancement observed all along below 650 K,
282 1-hexene oxidation initiated by O₃ was also studied at 300 K in an atmospheric pressure flow
283 reactor coupled with an orbitrap mass spectrometer equipped with a multi-scheme chemical
284 ionization inlet (O-MION-CIMS)^{41,42}. A gas mixture consisting of bath gas air with various
285 1-hexene and O₃ mole fractions was investigated in a TFR utilizing a moveable injector to
286 achieve reaction times between 1.5 and 9.2 s. As shown in Figure 2, several HOMs and less
287 oxygenated reaction products were promptly observed.

288

289
290
291
292
293
294
295
296
297

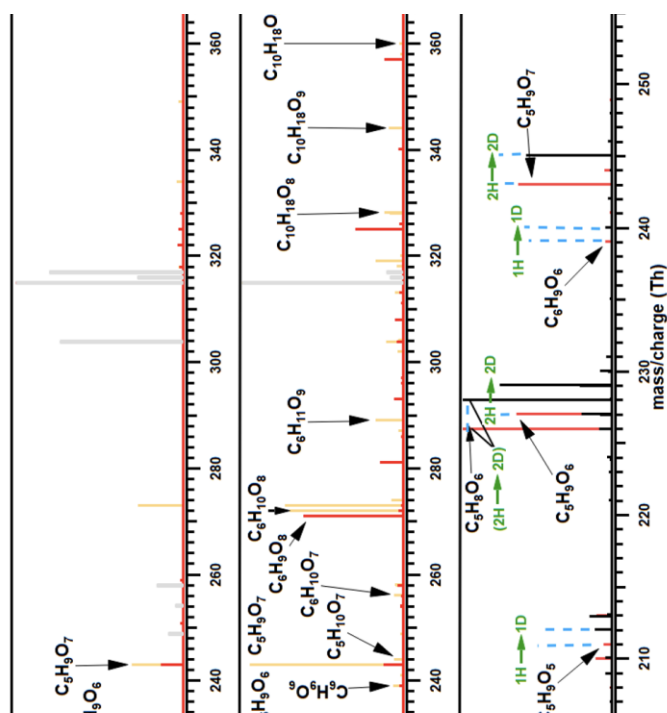
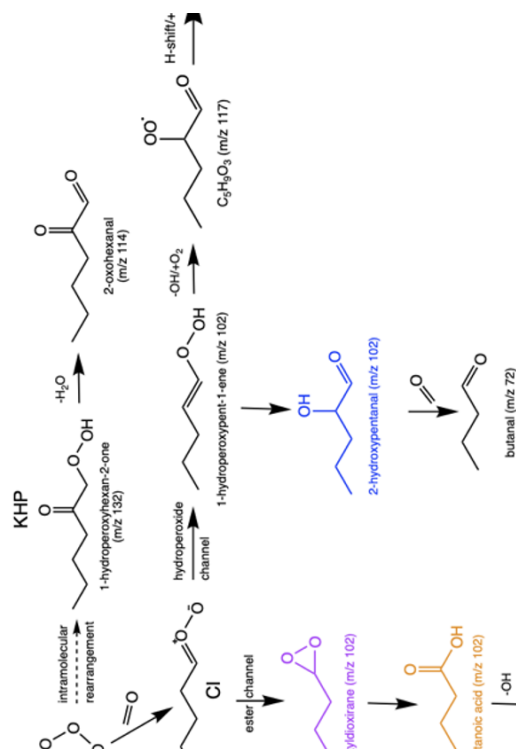


Figure 2. NO_3^- O-MION-CIMS mass spectra of 1-hexene + O_3 oxidation products. **A)** At 1.5 seconds reaction time with $[\text{C}_6\text{H}_{12}] = 0.5$ ppm (red) and $[\text{C}_6\text{H}_{12}] = 1.69$ ppm (yellow). **B)** At 9.2 seconds reaction time with $[\text{C}_6\text{H}_{12}] = 0.17$ ppm (red) and $[\text{C}_6\text{H}_{12}] = 1.69$ ppm (yellow). **C)** D_2O addition experiments showing the expected $\text{H} \rightarrow \text{D}$ substitution (see Figure 3). The inset shows the corresponding conversion of the reagent ion adducts $\text{HNO}_3 \cdot \text{NO}_3^-$ to $\text{DNO}_3 \cdot \text{NO}_3^-$ indicating the completeness of the H to D substitution. All spectra were measured at 300 K and atmospheric pressure of air with $[\text{O}_3] = 0.2$ ppm. The NO_3^- is omitted from the given product ion-adduct labels. Gray color is used to label background peaks.

298 Under the low ROO conversion regime, *i.e.*, short reaction time and low reactant
299 concentrations, the nitrate chemical ionization mass spectrum was dominated by a few
300 peroxy radicals formed by autoxidation, and their apparent unimolecular termination
301 products, *i.e.*, formed by an OH loss through abstraction from a carbon bearing an -OOH
302 group¹⁶. While both ROO from OH and O_3 initiated oxidation seemed to be apparent at
303 longer reaction times (Figure 2b), (*i.e.*, with 6 C-atoms indicating OH involvement and 5 C-
304 atoms signifying ozonolysis initiation, or a C-atom loss during the oxidation; Figure 3), the
305 dominance of the ozonolysis-initiated oxidation was apparent at short timescales (Figure 2a).
306 The most abundant ROO species observed was $\text{C}_5\text{H}_9\text{O}_7$ and its OH termination product
307 $\text{C}_5\text{H}_8\text{O}_6$, formed via a pseudo-unimolecular pathway shown in Figure 3, and supported by the
308 D_2O addition experiments (see Figure 3 and the SM). At longer residence times the
309 complexity quickly increases, leading to a multitude of radical and closed-shell reaction
310 products including the ROO accretion products ROOR with 10 C-atoms (Figure 2b). Also, a

311 $C_6H_9O_8$ radical becomes prominent, indicating the presence of cyclohexene^{51,52}, which was
 312 found as a minor impurity in the 1-hexene cylinder by a proton-transfer-reaction mass
 313 spectrometry (PTRMS) analysis.

314



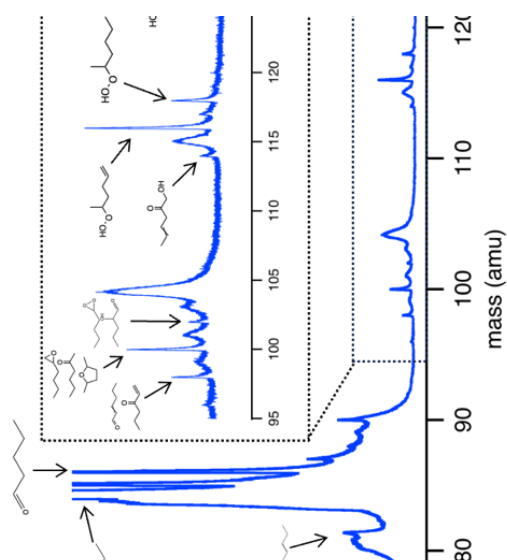
315
 316 **Figure 3.** Simplified reaction network of 1-hexene ozonolysis proposed in this work based on experimental
 317 observations. CI, KHP, and POZ refer to Criegee intermediates, ketohydroperoxides, and primary ozonide
 318 respectively. Dotted arrows refer to minor channels. The red circles indicate the H-atoms that were exchanged
 319 in the D_2O addition experiments (see Figure 2c and SM for more details).

320

321 1-hexene ozonolysis products in JSR

322 The study of 1-hexene + O_3 reaction between 350 K and 800 K in the JSR was also
 323 conducted with a i^2 PEPICO spectrometer available on the DESIRS VUV beamline at the
 324 SOLEIL synchrotron (see more experimental details in SM). Figure 4 displays a typical mass
 325 spectrum registered for a $He/O_2/1$ -hexene mixture at 400 K. The molecular structure of the
 326 chain-branching agents shown in Figure 4 was determined through the analysis of their
 327 mass-selected threshold photoelectron spectra (TPES) measured using mass spectrometer
 328 coupled with the i^2 PEPICO spectroscopy.

329

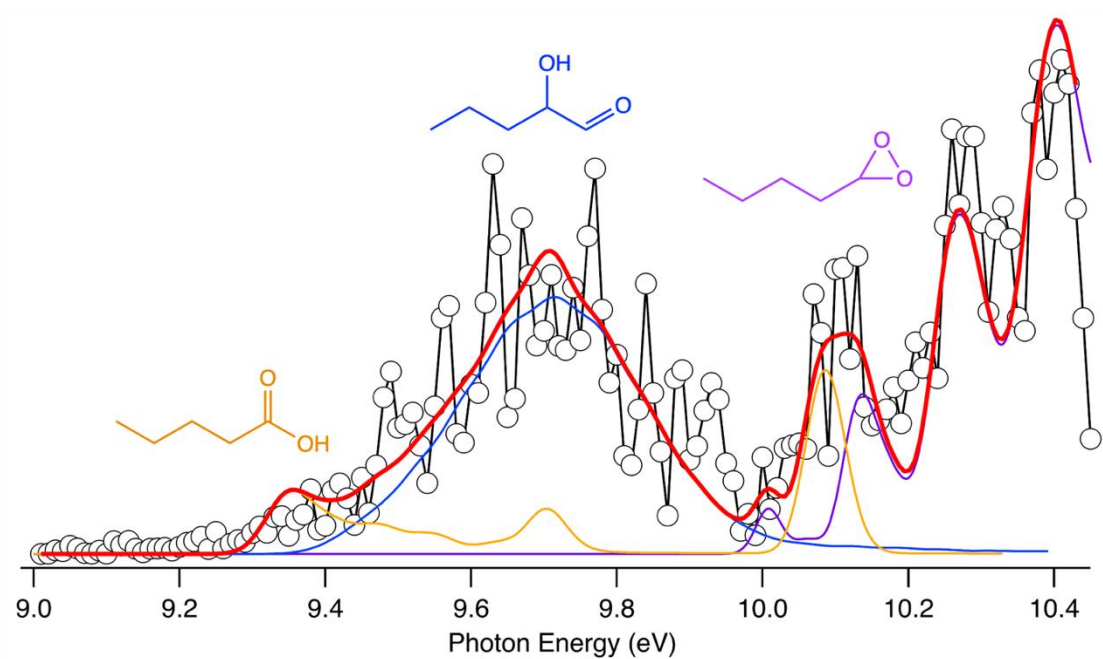


330
 331 **Figure 4.** Typical mass spectrum recorded by synchrotron VUV photoionization of a He/O₂/1-hexene gas mixture
 332 at 400 K with the addition of 3,000 ppm of O₃ (blue line). The mass spectrum is integrated over the 9.0–10.4 eV
 333 photon energy range. The inset shows a zoomed view of the expanded mass spectrum from 95 to 150 amu.
 334 Because the vertical scale is adjusted to emphasize the low-intensity peaks, that of 1-hexene (m/z 84) and of its
 335 7% ¹³C isotopologue (m/z 85) are truncated. The structures of some already-known products and intermediates
 336 based on the literature, are displayed along with combustion chain-branching agents that are the masses of
 337 interest that have been identified in this work. See text for details.

338
 339 Despite it was obtained at 400 K, the mass spectrum of Figure 4 reveals the presence
 340 products and intermediates both from the O₃-related kinetic network and from the LTC
 341 chemistry, which is expected to start only above 550 K. For instance, the hydroperoxides
 342 (m/z 116, 118, and 134) and ketohydroperoxides (m/z 130, 132, and 148) observed in Figure
 343 4 with alkenyl (AnHP/AnKHP) or hydroxyl (HyHP/HyKHP) functional groups are well known
 344 chain branching agents formed in the LTC of 1-hexene (see Figure S1)^{34,53}.

345 As shown in Figure S2 in SM, the TPES for m/z 116, 118, 130, and 148, and the total
 346 ion yield (TIY) of m/z 132 and 134, show good agreement with the simulated curves of the
 347 isomers in Figure 4 despite low signal-to-noise ratios and the complexity related to the
 348 simulation of vibronic transitions in floppy molecular systems⁵⁴. Note that the identification
 349 of the minor KHP, 5-hydroperoxyhexan-2-one, at m/z 132 is also validated by the presence
 350 of methyl ethyl ketone at m/z 72 as a product of the KHP decomposition (Figure S3),
 351 furthering confidence in the molecular structure findings.

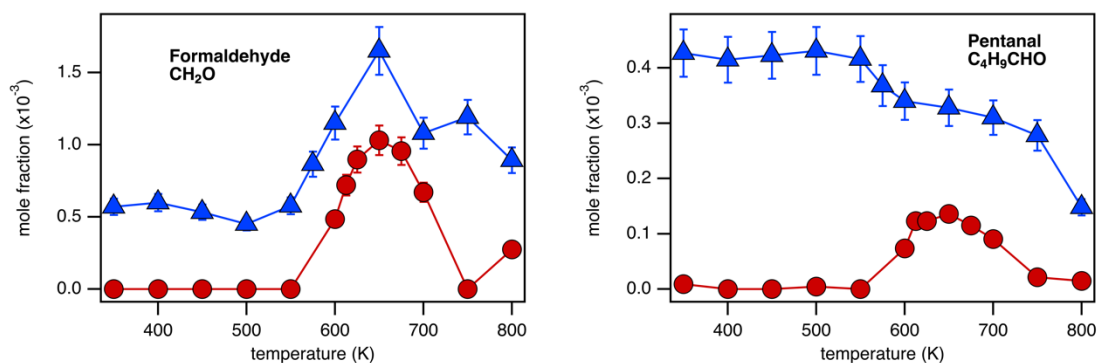
352



353
354
355
356
357
358

Figure 5. TPES of m/z 102 (open dots) compared to simulated PES of the isomers considered in this work: 3-butyldioxirane (purple line), 2-hydroxypentanal (blue line), and pentanoic acid (orange line). The thick red line is a weighed combination of the simulated spectra using a 0.4:1.0:0.3 signal ratio (2-hydroxypentanal, 3-butyldioxirane, pentanoic acid).

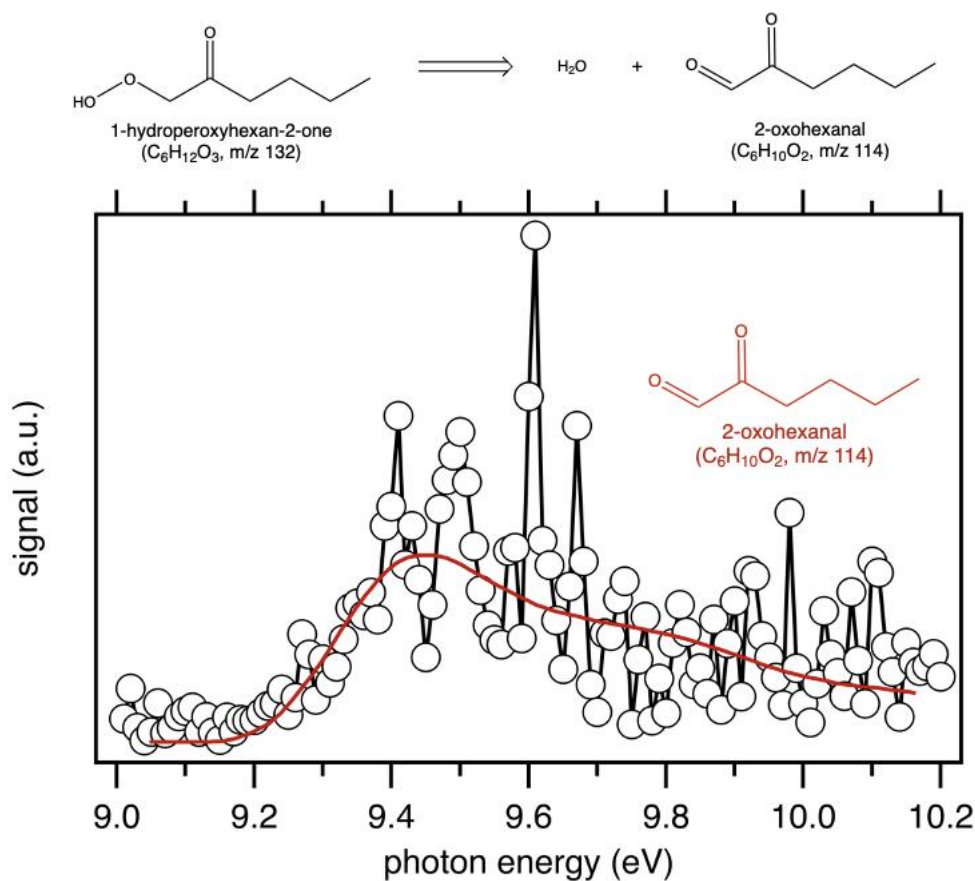
359 In 1-hexene ozonolysis oxidation, the formation of the primary ozonide (POZ), namely
360 4-butyl-1,2,3-trioxolane, dissociates into two reactive Criegee Intermediates (CIs): CH_2OO
361 and $\text{C}_4\text{H}_9\text{CHOO}$, as seen in Figure 3. These concurrent dissociations produce formaldehyde
362 (m/z 30) and pentanal (m/z 86) as co-products. The absence of a signal at m/z 30 in Figure 4
363 is due to the ionization energy of formaldehyde ($\text{IE} = 10.88 \text{ eV}$ ⁵⁵) which falls outside the
364 photon energy range explored in this study. Nevertheless, both formaldehyde and pentanal
365 were quantified in appreciable amounts using GC (see Figure 6). There is no formation of
366 both species without the introduction of O_3 below 550 K and this acts as a direct proof of the
367 ozonolysis mechanism.
368



369
 370 *Figure 6. Mole fraction of formaldehyde (left panel) and pentanal (right panel) recorded by GC as a*
 371 *function of temperature without (red circles) and with (blue triangles) the addition of O₃.*

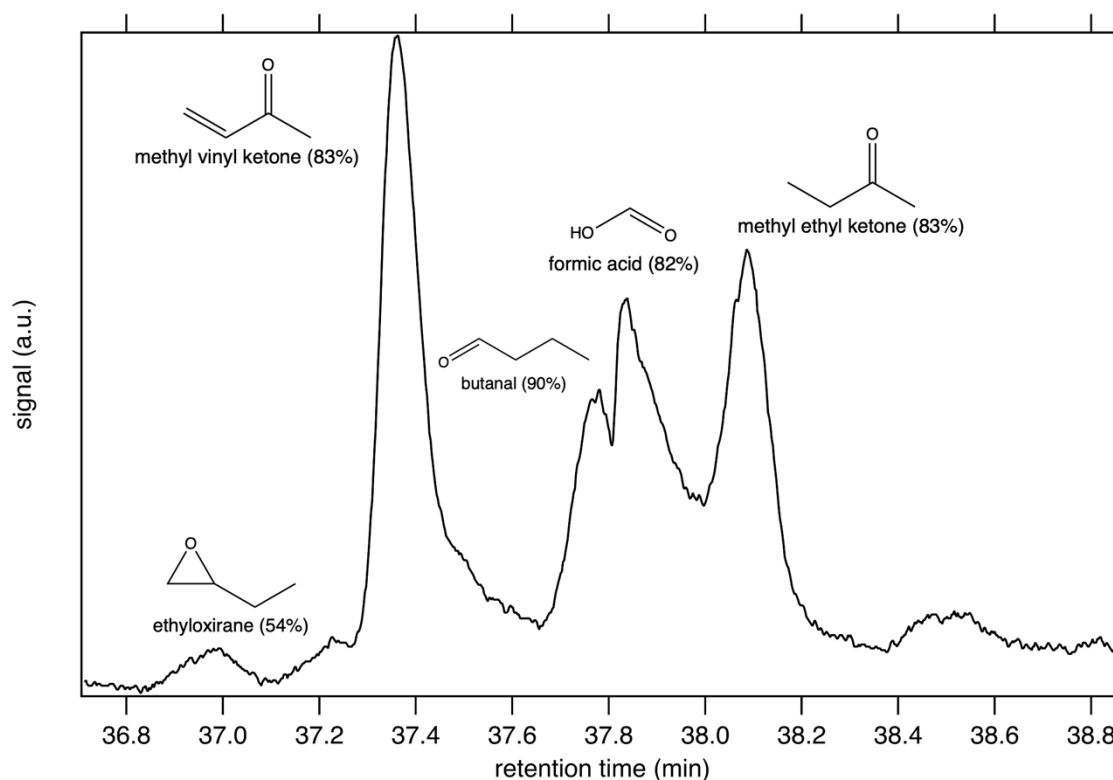
372
 373 Furthermore, this study highlights the detection of a KHP at m/z 132 stemming from
 374 POZ isomerization (see Figure 3) that has gained experimental validation only recently in
 375 ozonolysis systems^{56,57}. Besides the good agreement between the TIY of m/z 132 and the
 376 simulated one (see SI for theoretical details) for 1-hydroperoxyhexan-2-one in Figure S2,
 377 Figure 7 depicts a strong correlation between the experimentally recorded TPES of m/z 114
 378 and a simulated spectrum of 2-oxohexanal, the product of the decomposition of
 379 1-hydroperoxyhexan-2-one providing compelling evidence for its formation. Note that as
 380 expected due to their short lifetime, the POZ has not been detected in this study.

381



382
 383 *Figure 7. TPES of m/z 114 (open dots) compared to a simulated spectrum of 2-oxohexanal (red line). The*
 384 *chemical reaction shows the fragmentation mechanism of the KHP, 1-hydroperoxyhexan-2-one at m/z 132.*
 385

386 Formic acid (HCOOH, m/z 46) formed via the isomerization of the Cl CH₂OO into
 387 dioxirane intermediate (see Figure 3) has also been identified via GC-MS (see Figure 8), but
 388 quantification of HCOOH remained elusive due to its low FID signal⁵⁸. As for formaldehyde,
 389 no signal at m/z 46 has been recorded in Figure 4 because the AIE of HCOOH falls outside the
 390 photon energy range examined in this work (11.33 eV). Note that, due to the time
 391 restrictions typical of large facilities such as the SOLEIL synchrotron, the chosen photon
 392 energy range aimed to cover the ionization energy of most organic species.
 393

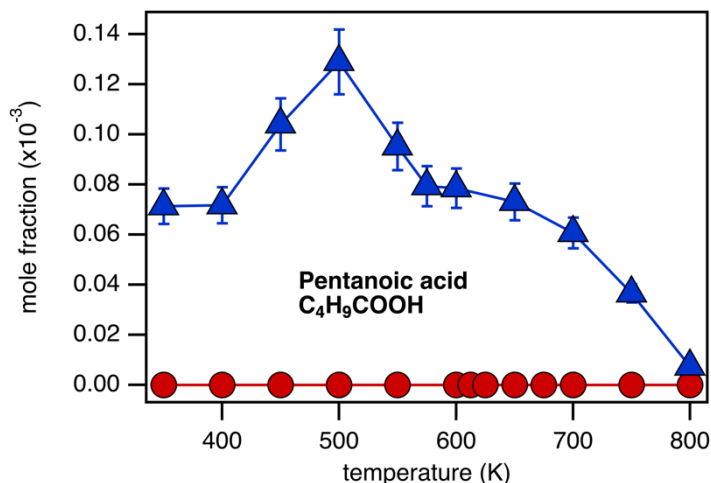


394
 395 *Figure 8. Chromatogram obtained at 650 K with the addition of O₃ showing the retention peak of formic acid*
 396 *along with other important oxidation products. The probability of match of each peak to the species according*
 397 *to the NIST database is provided based on the respective fragmentation pattern of each peak using a mass*
 398 *spectrometer with electron ionization.*
 399

400 In the gas-phase, due to the large exothermicity and the succession of weakly bound
 401 intermediates, the CI C₄H₉CHOO isomerization is thought to predominate. The CI is expected
 402 to isomerize promptly to 1-hydroperoxypent-1-ene, a vinylhydroperoxide (VHP) that is
 403 generally susceptible to dissociation into an organic oxygenated radical or subsequently
 404 isomerize into 2-hydroxypentanal, which then dissociates into butanal by losing a
 405 formaldehyde molecule. This oxygenated radical is the potential precursor to a sequence of
 406 reactions leading to HOM species detected in this work. However, the CI can also result in
 407 an oxirane, specifically 3-butyldioxirane, whose O-O bond cleavage can terminate in the
 408 formation of pentanoic acid. The TPES of m/z 102 is showcased in Figure 5 contrasted with
 409 simulated spectra of 3-butyldioxirane, 2-hydroxypentanal, and pentanoic acid. A least-
 410 squares fit of the simulated spectra to the TPES spectrum of m/z 102 reveals the presence of
 411 all the discussed species. The detection of pentanoic acid was also corroborated by GC (see

412 Figure 9) and acts also as another direct proof of the ozonolysis mechanism, as it is not
413 formed without the addition of O₃.

414



415

416 *Figure 9. Pentanoic acid mole fraction recorded by GC as a function of temperature without (red circles)*

417

and with (blue triangles) the addition of O₃.

418

419 Discussion

420 The results described in the previous part show that under combustion regime,

421 various hydroperoxide intermediates like KHPs are produced already at 300 K in 1-hexene

422 ozonolysis, indicating the formation of their parent OOQOOH radicals (for example, C₅H₉O₅

423 and C₅H₉O₇). The rate of the O₃-derived reactions, such as ROO H-shift isomerization, is likely

424 to increase significantly with temperature due to their substantial barriers enhancing the

425 quantity of oxygenated intermediates, and play a crucial role in shaping the autoxidation

426 behavior of 1-hexene. As temperature drops barrierless or low-barrier mechanisms are

427 favored such as OH-addition reactions to olefins⁵⁹. At the opposite, H-abstraction by OH

428 becomes increasingly competitive as temperature rises due to the increased energy at

429 higher temperatures, facilitating overcoming the activation barriers inherent to H-

430 abstraction reactions. This is illustrated by a decrease of the m/z 130/148 signal ratio by

431 around 50% at 400 K measured in Figure 4 compared to that measured in the LTC.^{60,61} The

432 LTC of 1-hexene is dominated by two pathways: H-abstraction and OH-addition onto the

433 double bond of the carbon chain leading respectively to m/z 130, an alkenyl

434 ketohydroperoxide and m/z 148, an hydroxyl ketohydroperoxide (see Figure S1). While the

435 H-abstraction is favored in the LTC, this result in this work emphasizing a shift in dominant
436 reaction pathways.

437 The O₃-related kinetic network operates up to at least 650 K and is responsible for
438 the observed 20% enhancement in the conversion of 1-Hexene when O₃ is added. This
439 increase is also a substantial contribution to the reactivity in the LTC region, even with the
440 KHP branching decomposition into OH and oxy (OO=O) radicals, enhancing much more the
441 overall combustion kinetics⁶². Propagation reactions from the O₃ side involving various
442 oxygenated intermediates increase the pool of radicals, especially OH with the loose O-OH
443 bonds, to trigger the LTC chemistry below 550 K. The species related to the LTC chemistry
444 found in Figure 4 are mainly initiated by the abstraction of allylic and alkylic H-atoms, the
445 addition of OH-radicals to the double bond, followed by the addition of an O₂ molecule. The
446 addition of H-atoms to create alkyl radicals (R) also play a role, but to a lesser extent as the
447 temperature is low (see Figure S1).

448 Importantly, the O-MION-CIMS measurements also show the detection of ROO
449 accretion products: ROOR'^{63,64} which have been found especially important for the
450 formation and growth of atmospheric SOA. While the accretion products were not found in
451 the PEPICO experiments, their involvement in shaping the autoxidation behavior of a VOC at
452 elevated temperature could also be substantial. They form very rapidly⁶⁵, the peroxide
453 bridge connecting the R units is weak, and the R units likely contain one or two relatively
454 weakly bound hydroperoxide functional groups each, potentially providing a cascade of
455 reactive radicals during decomposition contributing to increasing oxidation rate.

456 Out of the two CIs that are formed, C₄H₉CHOO is anticipated to have a more
457 significant impact than CH₂OO in increasing the concentration of radicals. The nascent
458 stabilization factor of CH₂OO is expected to be higher than C₄H₉CHOO because of the larger
459 size of the pentanal co-product which takes away more energy than formaldehyde⁶⁶.
460 However, this requires further theoretical analysis to determine the energy barriers
461 associated with isomerization and dissociation processes in this ozonolysis system, as well as
462 to calculate their respective branching ratios.

463 Beyond 650 K, the NTC zone begins because substantial quantities of poorly reactive
464 OOH radicals, which are produced through reactions like the concerted elimination (ROO =
465 olefin + HOO). However, this slowdown is expected to be counteracted by the thermal
466 decomposition of O₃ into O atoms, which affects the overall radical concentration and

467 balance in the system. The thermal decomposition of O_3 starts around 450-500 K and is
468 almost complete at the temperature of 650 – 700 K²⁷. The increase of 40% is twice the
469 increase observed at low temperatures likely due to the biradical nature of O atoms sharing
470 two radical sites ($O + RH \rightarrow R + OH$). The contribution of the much-accelerated $O_3 + 1$ -
471 hexene reaction in this region remain an opening question but is likely to be minimum
472 compared to the thermal decomposition of O_3 .

473 This work reveals the concurrent operation of two distinct yet intertwined chemical
474 systems where reaction mechanisms relevant to both atmospheric science and combustion
475 chemistry coexist. Radicals generated from ozonolysis spark a cascade of reactions
476 reminiscent of combustion processes at temperatures well below what they would be in the
477 absence of O_3 , establishing a distinct connection between atmospheric and combustion
478 chemistry. What is particularly noteworthy here is that these two chemical systems —
479 ozonolysis and combustion — do not interact. By looking at Figure 1, the fuel conversion
480 curves are the same except for a constant offset, up to the NTC region.

481

482 **Implications for Energy Efficiency, Atmospheric Sciences, and Pollution Control**

483 This work reports on the interplay of O_3 and the oxidation chemistry of 1-hexene
484 across a wide temperature range (300 – 800 K), connecting combustion engineering with
485 atmospheric science. The results emphasize an important discovery: O_3 enhances oxidation
486 and facilitates fuel conversion under typically inhibitory combustion conditions (<500 K and
487 > 700 K). The presence of O_3 expands the initially limited range of reactivity, covering
488 temperatures from those relevant to the atmosphere all the way up to those relevant to
489 combustion counteracting the NTC behavior.

490 At low combustion temperatures (< 550 K), ozonolysis initiates the LTC chemistry,
491 resulting in the formation of oxygenated reactive intermediates, including KHPs. These
492 findings support recent research emphasizing the significance of H-migration in ROO radicals
493 even at ambient atmospheric temperatures and in systems lacking the autocatalytic
494 influence of oxygen containing functional groups (i.e., pristine ROO radicals)⁶⁷⁻⁶⁹. The similar
495 sequence of reactions has been shown to lead to the formation of multitude of oxygenated
496 compounds, and ultimately HOMs, the fuel that drives atmospheric secondary organic
497 aerosol generation [4, 16]. Thus, the current results build an intriguing bridge between
498 atmospheric and combustion science: The same compounds that allow the embryonic

499 molecular clusters to grow into atmospherically relevant aerosol particles provide the spark
500 for igniting the formation of combustion intermediates at temperatures lower than has been
501 previously thought possible.

502 Specific combustion intermediates that are common in systems sequentially oxidizing
503 toward HOMs were here identified under intentionally increased O₃ concentrations but their
504 formation is unlikely to happen at typical ambient O₃ levels. To modify combustion
505 processes, significantly higher O₃ levels than those commonly found in the environment are
506 necessary, but these levels are not overly difficult to attain. Furthermore, current findings
507 suggest that for a comprehensive understanding of particle formation in areas with
508 temperature higher than in the troposphere and high O₃ concentrations, sometimes
509 exceeding ppm levels, such as in smoke plumes⁷⁰, the cooling exhausts of combustion
510 devices¹⁹, or even in certain megacities during intense pollution episodes⁷¹⁻⁷³, it is essential
511 to understand the processes resulting from both combustion and atmospheric chemistry.

512 From the industrial point of view, there is a growing interest in technologies based on
513 plasma-assisted combustion for the development of superior air-breathing engines⁷⁴ in
514 which O₃ can be formed in substantial amount, shading light on its potential as an efficient
515 fuel oxidation promoter¹⁹. The ability of O₃ to modify autoignition chemistry and trigger
516 unsaturated fuel autoxidation under conditions that are usually inhibitory multiplies the
517 interest in using O₃ in energy conversion devices, opening new possibilities ranging from the
518 refinement of fuel composition for optimization of current processes working at
519 intermediate combustion temperatures. The current research underscored a remarkable
520 influence of O₃ on the occurrence of NTC, that had been so far intuited in alkane oxidation
521 systems but with very limited effect^{24,25}. It also makes opportunities for the development of
522 new combustion techniques working at extremely low temperature and pollution mitigation
523 strategies.

524 By counteracting the NTC behavior and enabling more efficient fuel conversion across
525 a broader temperature range, engineers and scientists gain increased flexibility in designing
526 advanced energy conversion devices. This newfound flexibility means that temperature
527 constraints, which may have previously limited device development, are no longer a barrier.
528 Energy conversion devices can now be tailored and optimized for operation across a wider
529 spectrum of temperatures, offering a more adaptable and versatile approach.

530

531 **Conclusion**

532 This work highlights the dual role of O₃ at both low and high temperatures,
533 emphasizing its potential usefulness for fuel optimization and pollution reduction. Moreover,
534 the importance of atmospheric molecular mechanisms in triggering autoignition and
535 autoxidation under conditions that normally prevent it is also underlined. The combination
536 of two advanced analytical tools in mass spectrometry and spectroscopy has enabled the
537 detection of different species that are part of the same kinetic network; this suggests
538 promising prospects for using this analytical pairing to study even more complex chemical
539 systems.

540

541 **Acknowledgments**

542 We acknowledge SOLEIL for provision of synchrotron radiation under project
543 20210964 and we are grateful to J.-F. Gil for his technical help around the SAPHIRS set-up.
544 We thank the QUADMARTS International Research Network for promoting the collaboration.
545 This work was performed using HPC resources from the EXPLOR centre hosted by the
546 University of Lorraine (Project: 2021EXTXX2356). This project has received funding from the
547 European Research Council under the European Union's Horizon 2020 research and
548 innovation programme under Grant No. 101002728. The support from the Academy of
549 Finland (346373 and 353836) is greatly appreciated.

550

551 **References**

- 552 (1) Dec, J. E. Advanced Compression-Ignition Engines—Understanding the in-Cylinder
553 Processes. *Proceedings of the combustion institute* **2009**, 32 (2), 2727–2742.
- 554 (2) Pilling, M. J. *Low-Temperature Combustion and Autoignition*; Elsevier, 1997.
- 555 (3) Westbrook, C. K.; Mizobuchi, Y.; Poinso, T. J.; Smith, P. J.; Warnatz, J.
556 Computational Combustion. *Proceedings of the Combustion Institute* **2005**, 30 (1), 125–157.
- 557 (4) Ehn, M.; Thornton, J. A.; Kleist, E.; Sipilä, M.; Junninen, H.; Pullinen, I.; Springer,
558 M.; Rubach, F.; Tillmann, R.; Lee, B.; Lopez-Hilfiker, F.; Andres, S.; Acir, I.-H.; Rissanen,
559 M.; Jokinen, T.; Schobesberger, S.; Kangasluoma, J.; Kontkanen, J.; Nieminen, T.; Kurtén,
560 T.; Nielsen, L. B.; Jørgensen, S.; Kjaergaard, H. G.; Canagaratna, M.; Maso, M. D.; Berndt,
561 T.; Petäjä, T.; Wahner, A.; Kerminen, V.-M.; Kulmala, M.; Worsnop, D. R.; Wildt, J.;
562 Mentel, T. F. A Large Source of Low-Volatility Secondary Organic Aerosol. *Nature* **2014**,
563 506 (7489), 476–479. <https://doi.org/10.1038/nature13032>.
- 564 (5) Claeys, M.; Graham, B.; Vas, G.; Wang, W.; Vermeylen, R.; Pashynska, V.;
565 Cafmeyer, J.; Guyon, P.; Andreae, M. O.; Artaxo, P. Formation of Secondary Organic
566 Aerosols through Photooxidation of Isoprene. *Science* **2004**, 303 (5661), 1173–1176.
- 567 (6) Lelieveld, J. al; Butler, T. M.; Crowley, J. N.; Dillon, T. J.; Fischer, H.; Ganzeveld, L.;
568 Harder, H.; Lawrence, M. G.; Martinez, M.; Taraborrelli, D. Atmospheric Oxidation Capacity

569 Sustained by a Tropical Forest. *Nature* **2008**, *452* (7188), 737–740.
570 (7) Jokinen, T.; Berndt, T.; Makkonen, R.; Kerminen, V.-M.; Junninen, H.; Paasonen, P.;
571 Stratmann, F.; Herrmann, H.; Guenther, A. B.; Worsnop, D. R. Production of Extremely Low
572 Volatile Organic Compounds from Biogenic Emissions: Measured Yields and Atmospheric
573 Implications. *Proceedings of the National Academy of Sciences* **2015**, *112* (23), 7123–7128.
574 (8) J. Orlando, J.; S. Tyndall, G. Laboratory Studies of Organic Peroxy Radical
575 Chemistry: An Overview with Emphasis on Recent Issues of Atmospheric Significance.
576 *Chemical Society Reviews* **2012**, *41* (19), 6294–6317. <https://doi.org/10.1039/C2CS35166H>.
577 (9) Zádor, J.; Taatjes, C. A.; Fernandes, R. X. Kinetics of Elementary Reactions in Low-
578 Temperature Autoignition Chemistry. *Progress in Energy and Combustion Science* **2011**, *37*
579 (4), 371–421. <https://doi.org/10.1016/j.pecs.2010.06.006>.
580 (10) Savee, J. D.; Papajak, E.; Rotavera, B.; Huang, H.; Eskola, A. J.; Welz, O.; Sheps, L.;
581 Taatjes, C. A.; Zádor, J.; Osborn, D. L. Direct Observation and Kinetics of a
582 Hydroperoxyalkyl Radical (QOOH). *Science* **2015**, *347* (6222), 643–646.
583 <https://doi.org/10.1126/science.aaa1495>.
584 (11) Hansen, A. S.; Bhagde, T.; Moore, K. B.; Moberg, D. R.; Jasper, A. W.; Georgievskii,
585 Y.; Vansco, M. F.; Klippenstein, S. J.; Lester, M. I. Watching a Hydroperoxyalkyl Radical
586 (\bullet QOOH) Dissociate. *Science* **2021**, *373* (6555), 679–682.
587 <https://doi.org/10.1126/science.abj0412>.
588 (12) Curran, H. J. Developing Detailed Chemical Kinetic Mechanisms for Fuel
589 Combustion. *Proceedings of the Combustion Institute* **2019**, *37* (1), 57–81.
590 <https://doi.org/10.1016/j.proci.2018.06.054>.
591 (13) Griffiths, J. F. Negative Temperature-Coefficient of Reaction Rate during
592 Hydrocarbon Oxidation. *Journal of the Chemical Society D: Chemical Communications* **1969**,
593 No. 9, 483b–4484.
594 (14) Salooja, K. C. Zone of Negative Temperature Coefficient in Hydrocarbon Oxidation.
595 *Nature* **1960**, *185* (4705), 32–33. <https://doi.org/10.1038/185032a0>.
596 (15) Jenkin, M. E.; Valorso, R.; Aumont, B.; Rickard, A. R. Estimation of Rate
597 Coefficients and Branching Ratios for Reactions of Organic Peroxy Radicals for Use in
598 Automated Mechanism Construction. *Atmos. Chem. Phys.* **2019**, *19* (11), 7691–7717.
599 <https://doi.org/10.5194/acp-19-7691-2019>.
600 (16) Bianchi, F.; Kurtén, T.; Riva, M.; Mohr, C.; Rissanen, M. P.; Roldin, P.; Berndt, T.;
601 Crouse, J. D.; Wennberg, P. O.; Mentel, T. F.; Wildt, J.; Junninen, H.; Jokinen, T.; Kulmala,
602 M.; Worsnop, D. R.; Thornton, J. A.; Donahue, N.; Kjaergaard, H. G.; Ehn, M. Highly
603 Oxygenated Organic Molecules (HOM) from Gas-Phase Autoxidation Involving Peroxy
604 Radicals: A Key Contributor to Atmospheric Aerosol. *Chem. Rev.* **2019**, *119* (6), 3472–3509.
605 <https://doi.org/10.1021/acs.chemrev.8b00395>.
606 (17) Otkjær, R. V.; Jakobsen, H. H.; Tram, C. M.; Kjaergaard, H. G. Calculated Hydrogen
607 Shift Rate Constants in Substituted Alkyl Peroxy Radicals. *J. Phys. Chem. A* **2018**, *122* (43),
608 8665–8673. <https://doi.org/10.1021/acs.jpca.8b06223>.
609 (18) Møller, K. H.; Otkjær, R. V.; Chen, J.; Kjaergaard, H. G. Double Bonds Are Key to
610 Fast Unimolecular Reactivity in First-Generation Monoterpene Hydroxy Peroxy Radicals. *J.*
611 *Phys. Chem. A* **2020**, *124* (14), 2885–2896. <https://doi.org/10.1021/acs.jpca.0c01079>.
612 (19) Sun, W.; Gao, X.; Wu, B.; Ombrello, T. The Effect of Ozone Addition on
613 Combustion: Kinetics and Dynamics. *Progress in Energy and Combustion Science* **2019**, *73*,
614 1–25. <https://doi.org/10.1016/j.pecs.2019.02.002>.
615 (20) Liu, B.; Zhu, L.; Zhu, Q.; Lou, H.; Xu, Q.; Wang, Z. Ozone-Assisted Low
616 Temperature Oxidation of Methanol and Ethanol. *Applications in Energy and Combustion*
617 *Science* **2022**, *12*, 100085. <https://doi.org/10.1016/j.jaecs.2022.100085>.
618 (21) Liu, B.; Zhu, Q.; Zhu, L.; Hu, Z.; Xu, Q.; Wang, Z. Ozone-Initiated Low-Temperature

619 Oxidation of Two Propanol Isomers: Revealing the Effects of $\ddot{O}/\dot{O}H$ Atoms/Radicals.
620 *Combustion and Flame* **2023**, 256, 112956.
621 <https://doi.org/10.1016/j.combustflame.2023.112956>.

622 (22) Zhu, L.; Xu, Q.; Liu, B.; Xie, C.; Li, Y.; Wang, H.; Lou, H.; Zhu, Q.; Panigrahy, S.;
623 Curran, H.; Wang, Z.; Ju, Y.; Wang, Z. Ozone-Assisted Low-Temperature Oxidation of
624 Methane and Ethane. *Proceedings of the Combustion Institute* **2022**, S1540748922004278.
625 <https://doi.org/10.1016/j.proci.2022.09.052>.

626 (23) Zhu, L.; Xu, Q.; Xie, C.; Liu, B.; Wang, H.; Panigrahy, S.; Curran, H.; Wang, Z.
627 Chemical Insight into the Ozone-Assisted Low-Temperature Oxidation of Propane.
628 *Combustion and Flame* **2023**, 254, 112814.
629 <https://doi.org/10.1016/j.combustflame.2023.112814>.

630 (24) Liao, H.; Kang, S.; Hansen, N.; Zhang, F.; Yang, B. Influence of Ozone Addition on
631 the Low-Temperature Oxidation of Dimethyl Ether in a Jet-Stirred Reactor. *Combustion and*
632 *Flame* **2020**, 214, 277–286. <https://doi.org/10.1016/j.combustflame.2019.12.036>.

633 (25) Rouso, A. C.; Jasper, A. W.; Ju, Y.; Hansen, N. Extreme Low-Temperature
634 Combustion Chemistry: Ozone-Initiated Oxidation of Methyl Hexanoate. *J. Phys. Chem. A*
635 **2020**, 124 (48), 9897–9914. <https://doi.org/10.1021/acs.jpca.0c07584>.

636 (26) Conrad, A. R.; Hansen, N.; Jasper, A. W.; Thomason, N. K.; Hidalgo-Rodrigues, L.;
637 Treshock, S. P.; Popolan-Vaida, D. M. Identification of the Acetaldehyde Oxide Criegee
638 Intermediate Reaction Network in the Ozone-Assisted Low-Temperature Oxidation of *Trans*-
639 2-Butene. *Phys. Chem. Chem. Phys.* **2021**, 23 (41), 23554–23566.
640 <https://doi.org/10.1039/D1CP03126K>.

641 (27) Smith Lewin, C.; Herbinet, O.; Battin-Leclerc, F.; Bourgalais, J. Ozone-Assisted
642 Oxidation of Ethylene in a Jet-Stirred Reactor: An Experimental and Modeling Study.
643 *Chemical Physics Letters* **2022**, 806, 139986. <https://doi.org/10.1016/j.cplett.2022.139986>.

644 (28) Fan, H.; Ma, J.; Zhu, L.; Liu, B.; Liu, F.; Shan, X.; Wang, Z.; Wang, L. Unusual
645 Diradical Intermediates in Ozonolysis of Alkenes: A Combined Theoretical and Synchrotron
646 Radiation Photoionization Mass Spectrometric Study on Ozonolysis of Alkyl Vinyl Ethers. *J.*
647 *Phys. Chem. A* **2022**, 126 (43), 8021–8027. <https://doi.org/10.1021/acs.jpca.2c04382>.

648 (29) Rouso, A. C.; Hansen, N.; Jasper, A. W.; Ju, Y. Low-Temperature Oxidation of
649 Ethylene by Ozone in a Jet-Stirred Reactor. *J. Phys. Chem. A* **2018**, 122 (43), 8674–8685.
650 <https://doi.org/10.1021/acs.jpca.8b06556>.

651 (30) He, X.; Hansen, N.; Moshhammer, K. Molecular-Weight Growth in Ozone-Initiated
652 Low-Temperature Oxidation of Methyl Crotonate. *J. Phys. Chem. A* **2020**, 124 (39), 7881–
653 7892. <https://doi.org/10.1021/acs.jpca.0c05684>.

654 (31) Yang, S.; Wang, Q.; Curran, H. J.; Jia, M. Development of a 5-Component Gasoline
655 Surrogate Model Using Recent Advancements in the Detailed H₂/O₂/CO/C₁-C₃ Mechanism
656 for Decoupling Methodology. *Fuel* **2021**, 283, 118793.

657 (32) Cancino, L. R.; da Silva Jr, A.; De Toni, A. R.; Fikri, M.; Oliveira, A. A. M.; Schulz,
658 C.; Curran, H. J. A Six-Compound, High Performance Gasoline Surrogate for Internal
659 Combustion Engines: Experimental and Numerical Study of Autoignition Using High-
660 Pressure Shock Tubes. *Fuel* **2020**, 261, 116439.

661 (33) Yuan, H.; Chen, Z.; Zhou, Z.; Yang, Y.; Brear, M. J.; Anderson, J. E. Formulating
662 Gasoline Surrogate for Emulating Octane Blending Properties with Ethanol. *Fuel* **2020**, 261,
663 116243.

664 (34) Meng, X.; Rodriguez, A.; Herbinet, O.; Wang, T.; Battin-Leclerc, F. Revisiting 1-
665 Hexene Low-Temperature Oxidation. *Combustion and Flame* **2017**, 181, 283–299.
666 <https://doi.org/10.1016/j.combustflame.2017.03.031>.

667 (35) Herbinet, O.; Dayma, G. Jet-Stirred Reactors. In *Cleaner Combustion*; Battin-Leclerc,
668 F., Simmie, J. M., Blurock, E., Eds.; Green Energy and Technology; Springer London:

669 London, 2013; pp 183–210. https://doi.org/10.1007/978-1-4471-5307-8_8.

670 (36) Scanlon, J. T.; Willis, D. E. Calculation of Flame Ionization Detector Relative
671 Response Factors Using the Effective Carbon Number Concept. *Journal of Chromatographic*
672 *Science* **1985**, *23* (8), 333–340. <https://doi.org/10.1093/chromsci/23.8.333>.

673 (37) Tang, X.; Garcia, G. A.; Gil, J.-F.; Nahon, L. Vacuum Upgrade and Enhanced
674 Performances of the Double Imaging Electron/Ion Coincidence End-Station at the Vacuum
675 Ultraviolet Beamline DESIRS. *Review of Scientific Instruments* **2015**, *86* (12), 123108.
676 <https://doi.org/10.1063/1.4937624>.

677 (38) Nahon, L.; de Oliveira, N.; Garcia, G. A.; Gil, J.-F.; Pilette, B.; Marcouillé, O.;
678 Lagarde, B.; Polack, F. DESIRS: A State-of-the-Art VUV Beamline Featuring High
679 Resolution and Variable Polarization for Spectroscopy and Dichroism at SOLEIL. *J*
680 *Synchrotron Rad* **2012**, *19* (4), 508–520. <https://doi.org/10.1107/S0909049512010588>.

681 (39) Garcia, G. A.; Cunha de Miranda, B. K.; Tia, M.; Daly, S.; Nahon, L. DELICIOUS
682 III: A Multipurpose Double Imaging Particle Coincidence Spectrometer for Gas Phase
683 Vacuum Ultraviolet Photodynamics Studies. *Review of Scientific Instruments* **2013**, *84* (5),
684 053112. <https://doi.org/10.1063/1.4807751>.

685 (40) Poully, J. C.; Schermann, J. P.; Nieuwjaer, N.; Lecomte, F.; Grégoire, G.; Desfrancois,
686 C.; Garcia, G. A.; Nahon, L.; Nandi, D.; Poisson, L.; Hochlaf, M. Photoionization of 2-
687 Pyridone and 2-Hydroxypyridine. *Phys. Chem. Chem. Phys.* **2010**, *12* (14), 3566.
688 <https://doi.org/10.1039/b923630a>.

689 (41) Rissanen, M. P.; Mikkilä, J.; Iyer, S.; Hakala, J. Multi-Scheme Chemical Ionization
690 Inlet (MION) for Fast Switching of Reagent Ion Chemistry in Atmospheric Pressure
691 Chemical Ionization Mass Spectrometry (CIMS) Applications. *Atmospheric Measurement*
692 *Techniques* **2019**, *12* (12), 6635–6646.

693 (42) He, X. C.; Shen, J.; Iyer, S.; Juuti, P.; Zhang, J.; Koirala, M.; Kytökari, M. M.;
694 Worsnop, D. R.; Rissanen, M.; Kulmala, M. Characterisation of Gaseous Iodine Species
695 Detection Using the Multi-Scheme Chemical Ionisation Inlet 2 with Bromide and Nitrate
696 Chemical Ionisation Methods. *Atmospheric Measurement Techniques* **2023**, *16* (19), 4461–
697 4487.

698 (43) Halgren, T. A. MMFF VII. Characterization of MMFF94, MMFF94s, and Other
699 Widely Available Force Fields for Conformational Energies and for Intermolecular-
700 Interaction Energies and Geometries. *Journal of Computational Chemistry* **1999**, *20* (7), 730–
701 748. [https://doi.org/10.1002/\(SICI\)1096-987X\(199905\)20:7<730::AID-JCC8>3.0.CO;2-T](https://doi.org/10.1002/(SICI)1096-987X(199905)20:7<730::AID-JCC8>3.0.CO;2-T).

702 (44) Zhao, Y.; Truhlar, D. G. The M06 Suite of Density Functionals for Main Group
703 Thermochemistry, Thermochemical Kinetics, Noncovalent Interactions, Excited States, and
704 Transition Elements: Two New Functionals and Systematic Testing of Four M06-Class
705 Functionals and 12 Other Functionals. *Theor Chem Account* **2008**, *120* (1), 215–241.
706 <https://doi.org/10.1007/s00214-007-0310-x>.

707 (45) Kendall, R. A.; Dunning, T. H.; Harrison, R. J. Electron Affinities of the First- row
708 Atoms Revisited. Systematic Basis Sets and Wave Functions. *J. Chem. Phys.* **1992**, *96* (9),
709 6796–6806. <https://doi.org/10.1063/1.462569>.

710 (46) Grimme, S.; Antony, J.; Ehrlich, S.; Krieg, H. A Consistent and Accurate Ab Initio
711 Parametrization of Density Functional Dispersion Correction (DFT-D) for the 94 Elements H-
712 Pu. *J. Chem. Phys.* **2010**, *132* (15), 154104. <https://doi.org/10.1063/1.3382344>.

713 (47) Bloino, J. *Aiming at an accurate prediction of vibrational and electronic spectra for*
714 *medium- to- large molecules: An overview - Bloino - 2016 - International Journal of*
715 *Quantum Chemistry - Wiley Online Library*.
716 <https://onlinelibrary.wiley.com/doi/full/10.1002/qua.25188> (accessed 2021-06-07).

717 (48) Montgomery, J. A.; Frisch, M. J.; Ochterski, J. W.; Petersson, G. A. A Complete Basis
718 Set Model Chemistry. VI. Use of Density Functional Geometries and Frequencies. *J. Chem.*

719 *Phys.* **1999**, *110* (6), 2822–2827. <https://doi.org/10.1063/1.477924>.
720 (49) Montgomery, J. A.; Frisch, M. J.; Ochterski, J. W.; Petersson, G. A. A Complete Basis
721 Set Model Chemistry. VII. Use of the Minimum Population Localization Method. *J. Chem.*
722 *Phys.* **2000**, *112* (15), 6532–6542. <https://doi.org/10.1063/1.481224>.
723 (50) Mason, S. A.; Arey, J.; Atkinson, R. Rate Constants for the Gas-Phase Reactions of
724 NO₃ Radicals and O₃ with C₆–C₁₄ 1-Alkenes and 2-Methyl-1-Alkenes at 296 ± 2 K. *J.*
725 *Phys. Chem. A* **2009**, *113* (19), 5649–5656. <https://doi.org/10.1021/jp9014614>.
726 (51) Berndt, T.; Richters, S.; Kaethner, R.; Voigtländer, J.; Stratmann, F.; Sipilä, M.;
727 Kulmala, M.; Herrmann, H. Gas-Phase Ozonolysis of Cycloalkenes: Formation of Highly
728 Oxidized RO₂ Radicals and Their Reactions with NO, NO₂, SO₂, and Other RO₂ Radicals.
729 *J. Phys. Chem. A* **2015**, *119* (41), 10336–10348. <https://doi.org/10.1021/acs.jpca.5b07295>.
730 (52) Rissanen, M. P.; Kurtén, T.; Sipilä, M.; Thornton, J. A.; Kangasluoma, J.; Sarnela, N.;
731 Junninen, H.; Jørgensen, S.; Schallhart, S.; Kajos, M. K.; Taipale, R.; Springer, M.; Mentel,
732 T. F.; Ruuskanen, T.; Petäjä, T.; Worsnop, D. R.; Kjaergaard, H. G.; Ehn, M. The Formation
733 of Highly Oxidized Multifunctional Products in the Ozonolysis of Cyclohexene. *J. Am. Chem.*
734 *Soc.* **2014**, *136* (44), 15596–15606. <https://doi.org/10.1021/ja507146s>.
735 (53) Bourgalais, J.; Smith Lewin, C.; Herbinet, O.; Garcia, G. A.; Arnoux, P.; Tran, L.-S.;
736 Vanhove, G.; Nahon, L.; Battin-Leclerc, F. Refining the Chain-Branching Process in the
737 Low-Temperature Oxidation of 1-Hexene with Synchrotron-Based PEPICO Spectroscopy.
738 *Combustion and Flame* **2023**, *258*, 113065.
739 <https://doi.org/10.1016/j.combustflame.2023.113065>.
740 (54) Bourgalais, J.; Jiang, Z.; Bloino, J.; Herbinet, O.; Carstensen, H.-H.; Garcia, G. A.;
741 Arnoux, P.; Tran, L.-S.; Vanhove, G.; Nahon, L.; Battin-Leclerc, F.; Hochlaf, M. Accounting
742 for Molecular Flexibility in Photoionization: Case of Tert-Butyl Hydroperoxide. *Phys. Chem.*
743 *Chem. Phys.* **2022**, *24*, 10826. <https://doi.org/10.1039/D2CP00929C>.
744 (55) Linstrom, P. J.; Mallard, W. G.; Eds. *NIST Chemistry WebBook, NIST Standard*
745 *Reference Database Number 69*. National Institute of Standards and Technology,
746 Gaithersburg MD, 20899 (accessed 2023-01-10).
747 (56) Lewin, C. S.; Herbinet, O.; Garcia, G. A.; Arnoux, P.; Tran, L.-S.; Vanhove, G.;
748 Nahon, L.; Battin-Leclerc, F.; Bourgalais, J. Experimental Evidence for the Elusive
749 Ketohydroperoxide Pathway and the Formation of Glyoxal in Ethylene Ozonolysis. *Chem.*
750 *Commun.* **2022**, *58* (94), 13139–13142. <https://doi.org/10.1039/D2CC05229F>.
751 (57) Fan, H.; Ma, J.; Zhu, L.; Liu, B.; Liu, F.; Shan, X.; Wang, Z.; Wang, L. Unusual
752 Diradical Intermediates in Ozonolysis of Alkenes: A Combined Theoretical and Synchrotron
753 Radiation Photoionization Mass Spectrometric Study on Ozonolysis of Alkyl Vinyl Ethers. *J.*
754 *Phys. Chem. A* **2022**, *126* (43), 8021–8027. <https://doi.org/10.1021/acs.jpca.2c04382>.
755 (58) Spanjers, C. S.; Beach, C. A.; Jones, A. J.; Dauenhauer, P. J. Increasing Flame
756 Ionization Detector (FID) Sensitivity Using Post-Column Oxidation–Methanation. *Anal.*
757 *Methods* **2017**, *9* (12), 1928–1934. <https://doi.org/10.1039/C6AY03363F>.
758 (59) Zádor, J.; Jasper, A. W.; Miller, J. A. The Reaction between Propene and Hydroxyl.
759 *Phys. Chem. Chem. Phys.* **2009**, *11* (46), 11040. <https://doi.org/10.1039/b915707g>.
760 (60) Xie, C.; Xu, Q.; Chen, W.; Yu, T.; Wei, L.; Xing, L.; Wang, Z. Evaluating the Role of
761 Hydroxyl Keto-Hydroperoxide in the Low Temperature Oxidation of Alkenes. *Combustion*
762 *and Flame* **2022**, *246*, 112414. <https://doi.org/10.1016/j.combustflame.2022.112414>.
763 (61) Bourgalais, J.; Smith Lewin, C.; Herbinet, O.; Garcia, G. A.; Arnoux, P.; Tran, L.-S.;
764 Vanhove, G.; Nahon, L.; Battin-Leclerc, F. Refining the Chain-Branching Process in the
765 Low-Temperature Oxidation of 1-Hexene with Synchrotron-Based PEPICO Spectroscopy.
766 *Combustion and Flame* **2023**.
767 (62) Wang, Z.; Herbinet, O.; Hansen, N.; Battin-Leclerc, F. Exploring Hydroperoxides in
768 Combustion: History, Recent Advances and Perspectives. *Progress in Energy and*

769 *Combustion Science* **2019**, *73*, 132–181.
770 (63) Valiev, R. R.; Hasan, G.; Salo, V.-T.; Kubečka, J.; Kurten, T. Intersystem Crossings
771 Drive Atmospheric Gas-Phase Dimer Formation. *J. Phys. Chem. A* **2019**, *123* (30), 6596–
772 6604. <https://doi.org/10.1021/acs.jpca.9b02559>.
773 (64) Peräkylä, O.; Berndt, T.; Franzon, L.; Hasan, G.; Meder, M.; Valiev, R. R.; Daub, C.
774 D.; Varelas, J. G.; Geiger, F. M.; Thomson, R. J.; Rissanen, M.; Kurtén, T.; Ehn, M. Large
775 Gas-Phase Source of Esters and Other Accretion Products in the Atmosphere. *J. Am. Chem.*
776 *Soc.* **2023**, *145* (14), 7780–7790. <https://doi.org/10.1021/jacs.2c10398>.
777 (65) Berndt, T.; Scholz, W.; Mentler, B.; Fischer, L.; Herrmann, H.; Kulmala, M.; Hansel,
778 A. Accretion Product Formation from Self- and Cross- Reactions of RO₂ Radicals in the
779 Atmosphere. *Angew Chem Int Ed* **2018**, *57* (14), 3820–3824.
780 <https://doi.org/10.1002/anie.201710989>.
781 (66) Yang, L.; Campos-Pineda, M.; Hatem, K.; Zhang, J. Low-Pressure and Nascent Yields
782 of Stabilized Criegee Intermediates CH₂OO and CH₃CHOO in Ozonolysis of Propene.
783 *Phys. Chem. Chem. Phys.* **2023**, *25* (39), 26549–26556. <https://doi.org/10.1039/D3CP02590J>.
784 (67) Vereecken, L.; Nozière, B. H Migration in Peroxy Radicals under Atmospheric
785 Conditions. *Atmos. Chem. Phys.* **2020**, *20* (12), 7429–7458. [https://doi.org/10.5194/acp-20-](https://doi.org/10.5194/acp-20-7429-2020)
786 [7429-2020](https://doi.org/10.5194/acp-20-7429-2020).
787 (68) Seal, P.; Barua, S.; Iyer, S.; Kumar, A.; Rissanen, M. A Systematic Study on the
788 Kinetics of H-Shift Reactions in Pristine Acyl Peroxy Radicals. *Phys. Chem. Chem. Phys.*
789 **2023**, 10.1039.D3CP01833D. <https://doi.org/10.1039/D3CP01833D>.
790 (69) Barua, S.; Iyer, S.; Kumar, A.; Seal, P.; Rissanen, M. An Aldehyde as a Rapid Source
791 of Secondary Aerosol Precursors: Theoretical and Experimental Study of Hexanal
792 Autoxidation. *Atmos. Chem. Phys.* **2023**, *23* (18), 10517–10532. [https://doi.org/10.5194/acp-](https://doi.org/10.5194/acp-23-10517-2023)
793 [23-10517-2023](https://doi.org/10.5194/acp-23-10517-2023).
794 (70) Xu, L.; Crouse, J. D.; Vasquez, K. T.; Allen, H.; Wennberg, P. O.; Bourgeois, I.;
795 Brown, S. S.; Campuzano-Jost, P.; Coggon, M. M.; Crawford, J. H.; DiGangi, J. P.; Diskin,
796 G. S.; Fried, A.; Gargulinski, E. M.; Gilman, J. B.; Gkatzelis, G. I.; Guo, H.; Hair, J. W.; Hall,
797 S. R.; Halliday, H. A.; Hanisco, T. F.; Hannun, R. A.; Holmes, C. D.; Huey, L. G.; Jimenez, J.
798 L.; Lamplugh, A.; Lee, Y. R.; Liao, J.; Lindaas, J.; Neuman, J. A.; Nowak, J. B.; Peischl, J.;
799 Peterson, D. A.; Piel, F.; Richter, D.; Rickly, P. S.; Robinson, M. A.; Rollins, A. W.; Ryerson,
800 T. B.; Sekimoto, K.; Selimovic, V.; Shingler, T.; Soja, A. J.; St. Clair, J. M.; Tanner, D. J.;
801 Ullmann, K.; Veres, P. R.; Walega, J.; Warneke, C.; Washenfelder, R. A.; Weibring, P.;
802 Wisthaler, A.; Wolfe, G. M.; Womack, C. C.; Yokelson, R. J. Ozone Chemistry in Western
803 U.S. Wildfire Plumes. *Sci. Adv.* **2021**, *7* (50), eabl3648.
804 <https://doi.org/10.1126/sciadv.abl3648>.
805 (71) Li, K.; Jacob, D. J.; Shen, L.; Lu, X.; De Smedt, I.; Liao, H. Increases in Surface
806 Ozone Pollution in China from 2013 to 2019: Anthropogenic and Meteorological Influences.
807 *Atmos. Chem. Phys.* **2020**, *20* (19), 11423–11433. <https://doi.org/10.5194/acp-20-11423-2020>.
808 (72) Kalashnikov, D. A.; Schnell, J. L.; Abatzoglou, J. T.; Swain, D. L.; Singh, D.
809 Increasing Co-Occurrence of Fine Particulate Matter and Ground-Level Ozone Extremes in
810 the Western United States. *Sci. Adv.* **2022**, *8* (1), eabi9386.
811 <https://doi.org/10.1126/sciadv.abi9386>.
812 (73) Otero, N.; Sillmann, J.; Schnell, J. L.; Rust, H. W.; Butler, T. Synoptic and
813 Meteorological Drivers of Extreme Ozone Concentrations over Europe. *Environ. Res. Lett.*
814 **2016**, *11* (2), 024005. <https://doi.org/10.1088/1748-9326/11/2/024005>.
815 (74) Ju, Y.; Sun, W. Plasma Assisted Combustion: Dynamics and Chemistry. *Progress in*
816 *Energy and Combustion Science* **2015**, *48*, 21–83. <https://doi.org/10.1016/j.pecs.2014.12.002>.
817